JGR Solid Earth

RESEARCH ARTICLE
10.1029/2021JB022310

The Role of Along-Fault Dilatancy in Fault Slip Behavior

Yannick Caniven[1], **Julia K. Morgan**[1], and **David G. Blank**[1]

[1]Rice University, Houston, TX, USA

Key Points:

- A discrete element model is used to investigate earthquake nucleation mechanisms
- Fault geometry and precursory dilation/contraction patterns along strike might be predictive by controlling the earthquake energy balance
- Slow events in dilated zones bounded by neutral areas turn into earthquakes whereas those in alternating dilated/contracted zones stop

Supporting Information:

Supporting Information may be found in the online version of this article.

Correspondence to:

Y. Caniven,
ypc1@rice.edu

Citation:

Caniven, Y., Morgan, J. K., & Blank, D. G. (2021). The role of along-fault dilatancy in fault slip behavior. *Journal of Geophysical Research: Solid Earth*, *126*, e2021JB022310. https://doi.org/10.1029/2021JB022310

Received 12 MAY 2021
Accepted 21 OCT 2021

Author Contributions:

Data curation: Yannick Caniven
Formal analysis: Yannick Caniven, David G. Blank
Funding acquisition: Julia K. Morgan
Investigation: Yannick Caniven, David G. Blank
Methodology: Yannick Caniven, David G. Blank
Resources: Julia K. Morgan
Software: Julia K. Morgan
Supervision: Julia K. Morgan
Validation: Julia K. Morgan
Visualization: Yannick Caniven
Writing – original draft: Yannick Caniven
Writing – review & editing: Yannick Caniven, Julia K. Morgan, David G. Blank

Abstract

Earthquakes result from fast slip that occurs along a fault surface. Interestingly, numerous dense geodetic observations over the last two decades indicate that such dynamic slip may start by a gradual unlocking of the fault surface and related progressive slip acceleration. This first slow stage is of great interest, because it could define an early indicator of a devastating earthquake. However, not all slow slip turns into fast slip, and sometimes it may simply stop. In this study, we use a numerical model based on the discrete element method to simulate crustal strike-slip faults of 50 km length that generate a wide variety of slip-modes, from stable-slip, to slow earthquakes, to fast earthquakes, all of which show similar characteristics to natural cases. The main goal of this work is to understand the conditions that allow slow events to turn into earthquakes, in contrast to those that cause slow earthquakes to stop. Our results suggest that fault surface geometry and related dilation/contraction patterns along strike play a key role. Slow earthquakes that initiate in large dilated regions bounded by neutral or low contracted domains, might turn into earthquakes. Slow events occurring in regions dominated by closely spaced, alternating, small magnitude dilational and contractional zones tend not to accelerate and may simply stop as isolated slow earthquakes.

Plain Language Summary

Numerous research studies indicate that earthquakes may start progressively by a slow unlocking of the fault surface followed by fast slip acceleration. This first slow-slip stage could then define an early indicator of a devastating earthquake. However, not all slow-slip become fast, and some may simply stop. In this study, we use a numerical model to simulate faults that generate both slow earthquakes and fast earthquakes, sharing similar characteristics to natural cases. The main goal is to understand the conditions that allow slow events to turn into earthquakes, in contrast to those that cause slip to abort. Our results suggest that fault surface geometry and induced strain patterns play a key role. Slow events that initiate in large dilated regions might turn into earthquakes whereas the ones occurring in regions showing more complex strain pattern including contracted zones may simply stop as isolated inoffensive slow earthquakes. This work could have significant implications for the development of new monitoring systems devoted to anticipate the occurrence of destructive earthquakes.

1. Introduction

Numerous dense geodetic observations over recent decades reveal that faults can experience a wide range of slip velocities, ranging from stable slow aseismic creep to fast dynamic instability of earthquakes. In this spectrum of fault slip, slow earthquakes exhibit an intermediate behavior between purely steady aseismic creep and regular earthquakes (Hawthorne & Bartlow, 2018; Leeman et al., 2016; Miller et al., 2002).

We note that the term "slow earthquake" is not very well defined, and in fact has been used for various phenomena. Based on scaling relationships between seismic moment and rupture duration (Abercrombie et al., 1995), earthquakes might be considered as "slow' when they occur with unexpectedly long durations, thus possibly characterized by low slip velocity and/or rupture velocity (Abercrombie & Ekström, 2003). Recent advances in technology and monitoring over the last decades made it possible to refine event classifications within the slow earthquake family (Hawthorne & Bartlow, 2018; Ide et al., 2007). These include low-frequency earthquakes (LFEs), very LFEs, short-term slow-slip events (duration of days), long-term slow-slip events (months and years), and episodic tremors-slip events (ETS; Barbot, 2019; Leeman et al., 2016; Obara & Kato, 2016; Tokuda & Shimada, 2019). They have been mostly detected at subduction zones (Frank et al., 2014; Radiguet et al., 2012; Zigone et al., 2012) and in strike-slip tectonic settings (Rousset et al., 2019; Shelly, 2010; Wei et al., 2013). In this paper, we use the term "slow earthquake" to refer to the whole range of slip-rates comprised between the steady background loading rate (tectonic plate rate) and the experimentally inferred seismic threshold of 1 m/s (Di Toro et al., 2004).

Interestingly, some observations indicate that slow earthquakes can occur prior to large earthquakes (Ruiz et al., 2014; Tokuda & Shimada, 2019), suggesting that they may play a role in earthquake initiation. As an example, such precursory slow motion was detected beginning 17 days before the occurrence of the 2014 Iquique Mw 8.1 subduction earthquake (Ruiz et al., 2014). During this period, continuous GPS stations located along the coast indicated progressive motion up to 10 mm trenchward, in contrast to the expected inland-directed interseismic motion. From this geodetic signal, the inverted aseismic slip distribution on the subduction interface indicated maximum slip values close to 1 m. Investigating a longer observation time-scale before the main shock, Socquet et al. (2017) even revealed an 8 month long precursory slow-slip, corresponding to an 80% aseismic Mw 6.5 event. In addition, a major change in plate convergence rate was detected in the same region by GPS stations in 2005, recording a decrease in trenchward velocity of ~20% (Ruiz et al., 2014). This apparent decrease in interseismic loading suggests that a large slow-slip event occurred almost 10 years before the 2014 mainshock, perhaps denoting a decadal scale phenomenon.

Slow slip sequences have also been observed in other regions and in various tectonic settings as single isolated events, that is, simply stopping without leading to any dynamic acceleration. Some of these occurred in cycles of repeated aseismic events (Gomberg, 2010; Wallace, 2020). Typical examples of this category of events occur along the 130 km central creeping segment of the San Andreas Fault (Khoshmanesh & Shirzaei, 2018). Slow-slip events of this region are observed over the entire seismogenic depth, from the brittle-ductile transition to the surface (Khoshmanesh & Shirzaei, 2018; Nadeau & McEvilly, 2004).

Periodic slow earthquakes are also observed along the central part of the fault where velocity-strengthening conditions are expected in this zone due to the presence of both weak materials (Lockner et al., 2011) and inferred high pore-pressure (Khoshmanesh & Shirzaei, 2018). This suggests that other factors may play a defining role in determining the ultimate slip behavior of faults, in addition to the rate-and-state friction law parameters often used to describe fault-slip stability (Scholz, 1998).

Numerous studies have revealed possible interactions between fluid and thermal processes such as shear heating, fluid pressure, inelastic pore creation, and fault slip (Bizzarri & Cocco, 2006; Lapusta et al., 2000; Segall et al., 2010; Segall & Bradley, 2012; Suzuki & Yamashita, 2014; Urata et al., 2012) and have considerably advanced our understanding of the controls on various fault slip modes. However, they do not yet provide a clear physical explanation of the processes and conditions that differentiate precursory slow-slip of earthquakes and isolated slow earthquakes.

One factor that has been only minimally studied to date is the role of strength heterogeneities related to geometrical asperities along the fault. Several studies have suggested that fault zone structure (Kirkpatrick et al., 2021) and fault roughness itself could play a key role on the frictional slip behavior (Renard & Candela, 2017; Tal et al., 2020). Furthermore, recent studies including numerical models (Blank & Morgan, 2019; Fournier & Morgan, 2012; Romanet et al., 2018; Tal et al., 2020), frictional experiments (Harbord et al., 2017), and analog models (Caniven et al., 2017) show that fault slip stability may be largely controlled by geometrical heterogeneity along the fault. As these models and experiments do not consider fluids and temperature effects, we argue that fluids and thermal pressurization (e.g., Segall & Bradley, 2012; Suzuki & Yamashita, 2014) alone may not be sufficient to explain the wide range of observed slip velocities in the nature. However, they may interact with other properties such as fault roughness through shear-induced dilatancy.

Using a particle-based model, Blank and Morgan (2019) proposed that the precursory behavior results from the gradual unlocking of geometrical asperities as the fault dilates prior to the earthquake. Although not yet systematically confirmed for natural cases (Main et al., 2012), the existence of such precursory dilatancy has been suggested from field studies (Frank, 1965; Mead, 1925), laboratory experiments (Nur, 1972), and theoretical developments (Freudenthal, 1975; Scholz et al., 1973).

In this paper, we use a numerical model based on the discrete element method (DEM) that allows for explicit investigations of processes that may play a role in fault slip mechanics and frictional behavior. Here, we address especially the following questions: (a) How does fault roughness and induced dilatancy control fault slip stability? (b) What are the geometrical configurations for which a slow earthquake might stop, resulting in an isolated event, versus one that leads to dynamic instability and earthquake?

Note that, the numerical slow earthquakes produced by our model exhibit slip rates in the order of 10^{-11} m/s, that is, technically at the upper end of the natural slow-earthquakes spectrum earlier defined in the introduction. Considering the broad range of slip rates produced in the model, we define events as "slow earthquakes" as long as they are under the seismic threshold (1 m/s). We discuss the interpretation of our numerical absolute slip rate values in the Discussion in the context of the limits and the capabilities of our modeling approach.

2. Methodology and Model Setup

We use a particle-based numerical modeling approach referred to as the DEM. The approach treats the material as an assemblage of separate blocks or particles, iteratively solving the equations of motion through finite difference, for discrete bodies with deformable contacts. A complete description of the DEM method is introduced by Cundall and Strack (1979) and RICEBAL, the code used here, is detailed in Morgan (2015). The potential of the approach also has been illustrated in previous works such as Blank et al. (2021), Blank and Morgan (2019), and Fournier and Morgan (2012), which also simulated earthquake processes. One of the main advantages of the DEM method is that it allows large displacements between the particles, unlike boundary element method for which equations are derived in the small-strain approximation, then in linear elasticity (Romanet et al., 2020). Here, the DEM employs elasto-frictional contacts assigned between particles, providing a nonlinear force-displacement relationships. This deals with finite material elasticity without introducing unrealistic artificial stress concentrations along the fault. As a consequence, unlike the boundary element method, the asperities in contact can slide past other each other. This is especially useful for investigating the micromechanical processes that control the deformation of bulk materials that fracture and fault.

DEM models have been successfully used to simulate geological deformation processes from the grain scale to crustal structures. The method has been applied to long time-scale systems such as accretionary prism and fold and thrust belt growth (Dean et al., 2013; Morgan, 2015), but also to short time-scale fault-rupture propagation during earthquakes (Blank et al., 2021; Blank & Morgan, 2019; Ferdowsi et al., 2013; Fournier & Morgan, 2012; Gao et al., 2018). The appeal of the method is that emergent faults that develop in such systems of discrete particles are characterized by heterogeneous and rough fault surfaces that can evolve through complex strain and stress paths, consistent with natural materials. Results from these models show coseismic slip gradients, slip-velocities and accelerations, consistent with typical values inferred from geodetic and seismological data (Blank & Morgan, 2019; Fournier & Morgan, 2012).

In this study, we simulate a vertical crustal strike-slip fault in two dimensions, viewed from the top. The model consists of a 2D assemblage of about 14,000 particles, bonded to impart cohesion at all contacts except along a pre-defined fault line of 50 km length, centered within a 30 km wide domain (Figure 1). To minimize boundary effects, the domain has periodic lateral boundaries, such that particles exiting the domain on one side, enter the opposite boundary to remain within the system.

The tensile and shear strengths of the bonds are set to prevent bond breakage in order to localize deformation along the fault. Thus, no plastic deformation, such as new faults and fractures, develops elsewhere within the domain. Detailed properties of particles and bonds can be found in the Supporting Information S1 (Table S1). The resulting bulk shear modulus is close to 10 GPa, which is on the order of typical crustal rocks. Four particle sizes are used to construct two distinct domains: (a) an outer domain composed of relatively coarse particles, and (b) a central fault domain ∼5 km wide around the fault line. Within the outer domain, the radii are 375 and 500 m with abundances of 50% each. Within the fault domain, the particle's radii are 75 and 100 m, with abundances of 50% each. The use of large particle sizes in the outer domain reduces calculation times with little impact on the mechanical behavior of the fault zone domain. No plastic deformation occurs away from the fault zone, so the outer domain transmits far-field elastic stresses from the boundary of the system to the fault.

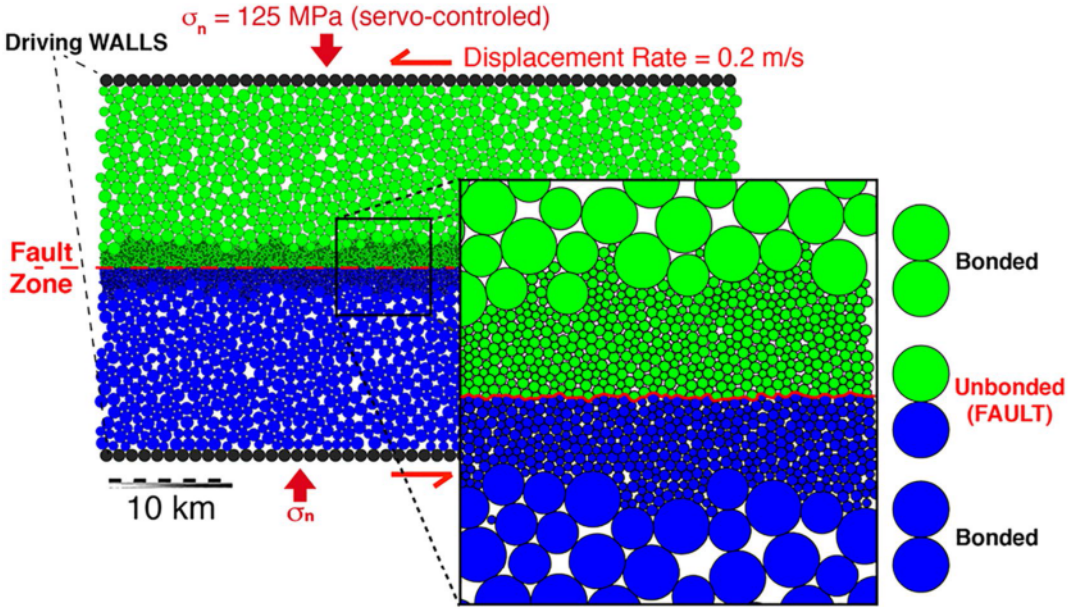

Figure 1. Model setup. Bonds are applied between all particles except between blue and green ones along a predefined fault interface. Here, the fault line geometry is uncontrolled and is referred to as a Random rough Interface Model.

For each of these two domains, the locations of particles are randomly generated. Then, the whole system is consolidated by applying a normal stress of 125 MPa to the rigid boundaries to reproduce a lithostatic pressure at around 5 km depth. After the consolidation stage, bonds are applied between all particles except along a prescribed horizontal fault line within the fault domain. The material properties on either side of the fault are similar and an interparticle friction coefficient μ_p of 0.2 is assigned everywhere in the domain. To shear the system, a constant velocity of 0.2 m/s is then imposed at the walls of the fault blocks, inducing a general strike-slip fault tectonic loading.

For this study, we construct four different fault interface models: (a) a Random rough Interface Model (RI Model) generated by partitioning randomly positioned particles into two wall domains on either side of the straight fault line, (b) a Controlled Fault Model (CF Model) bounded by two rows of uniformly space particles of 75 m radius, (c) a CF Model bounded by two rows of uniformly spaced particles of two different radii, 100 and 75 m, and (d) a CF Model bounded by two rows of uniformly spaced particles of two different radii, 200 and 75 m. The objective behind the four fault interface configurations is to examine their dilational behaviors during shear, and to relate these to fault slip behaviors. The RI Model is expected to yield heterogeneous dilation with slip depending on the relative positions of particles on either side of the fault. In contrast, the three CF Models should exhibit periodic behavior governed by the relative particle sizes in the interacting particle rows. Of these three configurations, the fault defined by matching particle radii will exhibit the greatest dilation as the two rows of particles alternate between square (loose) packing and hexagonal (close) packing arrangements. The high contrast in particle sizes in the final model will result in the lowest dilation.

Particle motions are derived from the sum of all contact forces components acting on each particle considering net force, displacement, moment of inertia, linear acceleration, and angular acceleration (Morgan, 2015). To dissipate energy in the system, and to mimic inelastic deformation in the earth, we impose a fractional damping of particle velocities, also called "viscous damping" (Cundall, 1987), which contributes to seismic wave attenuation.

Strain and stress fields in the models are derived from changes in particle positions over increments of time, and are calculated following procedures detailed by Morgan (2015). In the presented runs, the data are collected every 60 iterations of a 0.008 s time-step, corresponding to 0.48 s and to 9.6×10^{-12} m of relative wall displacements. This gives us complete access to the dynamics of the system from the seismic wave propagation time-scale to that of multiple earthquake cycles. We examine strain and stress patterns in two ways: (a) along the boundaries of the system, that is, far-field, and (b) immediately adjacent to the fault. In the first case, we plot ratios of shear stress to normal stress (τ/σ_n) acting on the rigid but displacing bounding walls, and also, assuming negligible local rotations, dilatancy of the system ($\delta y/\delta x$) derived from the normal wall displacements required to maintain constant normal stress.

The near fault data are given by time-space maps from stacked slip-velocity (V) and incremental volumetric strain ($\Delta\varepsilon_v$) profiles along the fault through time. The incremental volumetric strain field through the domain is calculated from particle displacements and derived strain components using

$$\Delta\varepsilon_v = \Delta\varepsilon_{xx} + \Delta\varepsilon_{yy} + \left(\Delta\varepsilon_{xx} \times \Delta\varepsilon_{yy}\right)$$

with x the along-fault direction, and y the direction orthogonal to the fault line. More details about the data processing can be found in the Supporting Information S1 (Text S4).

3. Results

3.1. Random Interface Model

The simulation run on the RI Model (Figure 1) produces a great variety of slip behavior, from aseismic transient creep to fast dynamic earthquakes (Figure 2). Time-space map plots reveal a highly complex spatiotemporal evolution of slip velocity (Figure 2a) and associated fault dilation (Figure 2b). Figure 2c illustrates such spatiotemporal variability in a statistical plot of slip-velocity values of all nodes displayed in Figure 2a. Fast events, or earthquakes (Eq), occur sporadically, sometimes rupturing only short stretches of the fault zone (e.g., Eq1, Eq2, Eq3, and Eq6), yet occasionally breaking the full length of the fault (Eq4 and Eq5). See the Movie S1 in Supporting Information S1 (Caniven et al., 2021) that illustrates the evolution of particle displacements at the global model scale during the fast Eq4 earthquake sequence. To first order, the regions of fast events (Eq1, Eq3, Eq4, Eq5, and Eq6) are preceded by precursory slow-slip and fault dilation, however, slower earthquakes (Eq2) and isolated slow earthquakes (SEq) with more complex volumetric strain patterns are also observed (Figures 2a and 2b). At the boundaries of the system, the recorded strain and stress at the wall also reveal a complex behavior during the experiment (Figure 2d). The evolution of stress ratio (τ/σ_n) with time exhibits an irregular seismic cycle consisting of multiple stress drops ($\Delta\tau$) varying in size and rate. Large and fast earthquake sequences that break the whole fault (Eq4 and Eq5) are preceded by incremental increases in wall expansion ($\delta y/\delta x$) in the y direction followed by large stress drops. Generally, such precursory dilation of the system appears proportional to stress-drop; that is, the larger rupture size, the larger the precursory dilation that can be detected at the system's boundary. However, all earthquakes with high maximum slip-velocities are preceded by measurable system dilation, which makes it difficult to discern the exact relationship between $\delta y/\delta x$ and $\Delta\tau$ with V. Events Eq3 and Eq6 illustrate this ambiguity, experiencing very fast slip similar to Eq4 and Eq5 ($V_{\max} > 100$ m/s), but exhibiting only small stress drops and slight precursory dilation, barely detectable at the wall of the system (Figure 2d).

Thus, upon initial examination, system dilation during the precursory stages of earthquakes appears to be a potential indicator of the size of upcoming events (i.e., rupture length and slip amount). Local dilation along the fault also appears to denote the future locations of earthquakes. However, the relationships between dilation and maximum slip-velocity are not straightforward in this example. The mechanical interactions between the numerous geometrical asperities along the fault induce complex strain patterns that render difficult the identification of trends beyond the first order. Hence, before we carry out any further analyses with this RI Model, we investigate the simpler CF Models to first clarify the basic geometric controls of fault on fault slip behavior.

3.2. High Dilatancy Controlled Fault Model

Figure 3 exhibits time-space maps of the fault slip velocity and incremental volumetric strain along the fault for the high dilatancy CF Model case. This model produces large earthquakes that rupture the entire fault length with constant recurrence intervals. Figures 3a and 3b display two of the earthquake cycles produced by this model and Figures 3c and 3d detail one of these events. It reveals that these large fault ruptures nucleate at $x = 31$ km through progressive acceleration of slip, propagate laterally to an adjacent segment at

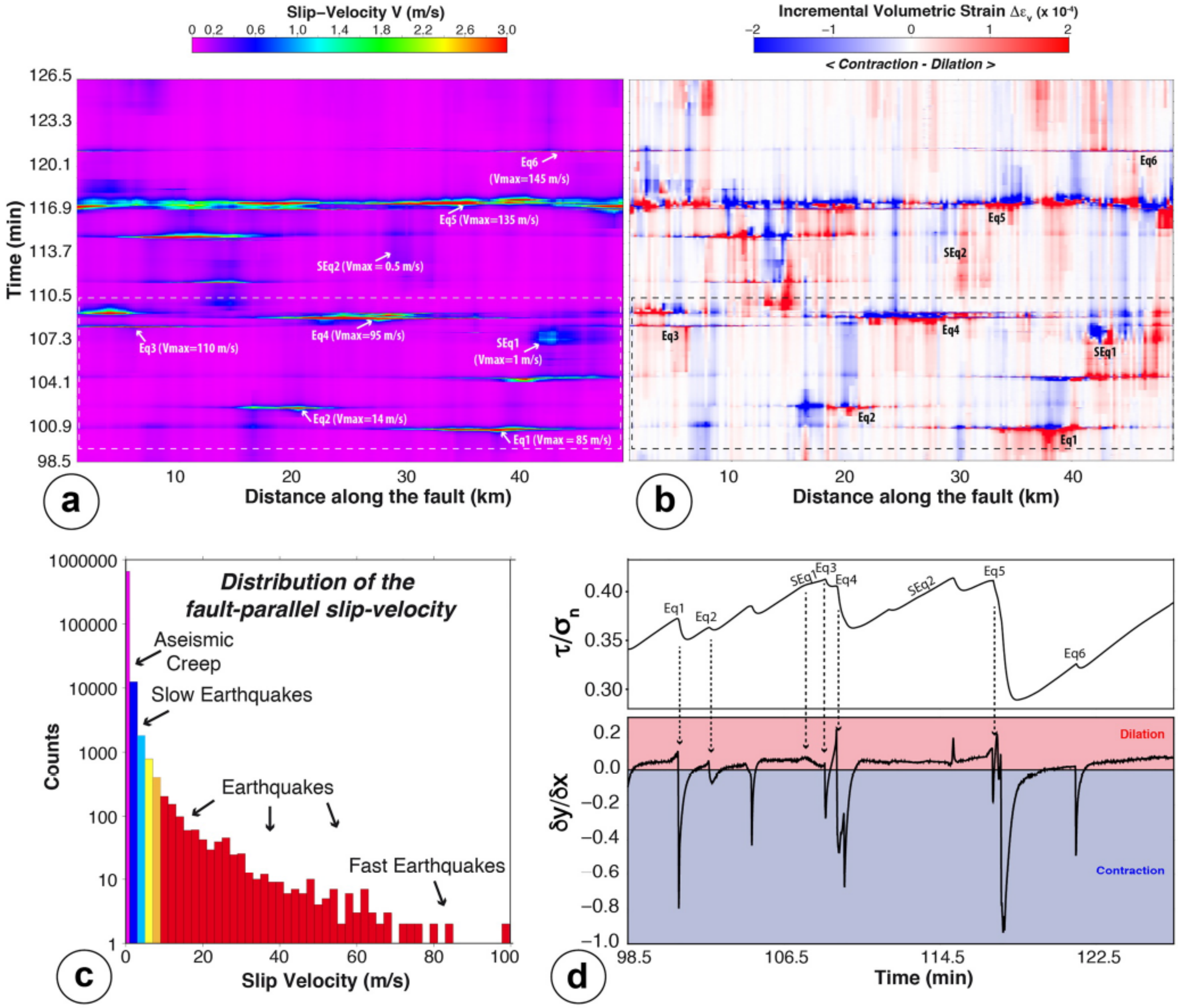

Figure 2. (a) Time-space map of the fault-parallel slip velocity obtained with the rough interface model and (b) related incremental volumetric strain. Eq = Earthquake; SEq = Slow Earthquake. (c) Statistical distribution of the along fault slip velocity for all data nodes from the time-space map in panel (a). Spatiotemporal resolution implies distance of 250 m between each node value along the fault, recorded every 0.48 s (see more details about data processing in Supporting Information S1, Text S4). (d) Stress ratios (τ/σ_n) and corresponding contraction-dilation ($\delta y/\delta x$) patterns of the system measured at the wall.

$x = 19$ km where slow nucleation was simultaneously going on, and then encompass the entire fault zone. Both of these zones of precursory slip also exhibit high dilation (red) well before the velocity peaks, marking the onset of a contractive stage (blue) associated with fault relocking. The maximum slip velocity along the fault, V_{max}, reaches ~70 m/s.

The relationship between volumetric strain and fault slip velocity is examined in more detail in Figure 4. Each white curve and associated gray squares plot the progressive evolution of V and $\Delta\varepsilon_v$ along a 250 m wide column of the time-space maps of Figures 3c and 3d. All curves follow clockwise circuits showing dilation during initial acceleration, followed by contraction as the peak slip velocity is achieved, and continued contraction through deceleration. The two colored curves capture this evolution at the two sites that exhibit the most precursory dilation and associated slow-slip. Interestingly, the magnitude of precursory dilation broadly correlates with the slip-velocity achieved during the subsequent contraction stage. Furthermore, during the earliest stages of dilation, regions experiencing the highest dilation rates are more prone to break with the highest fault slip-velocity (Figure 4, inset).

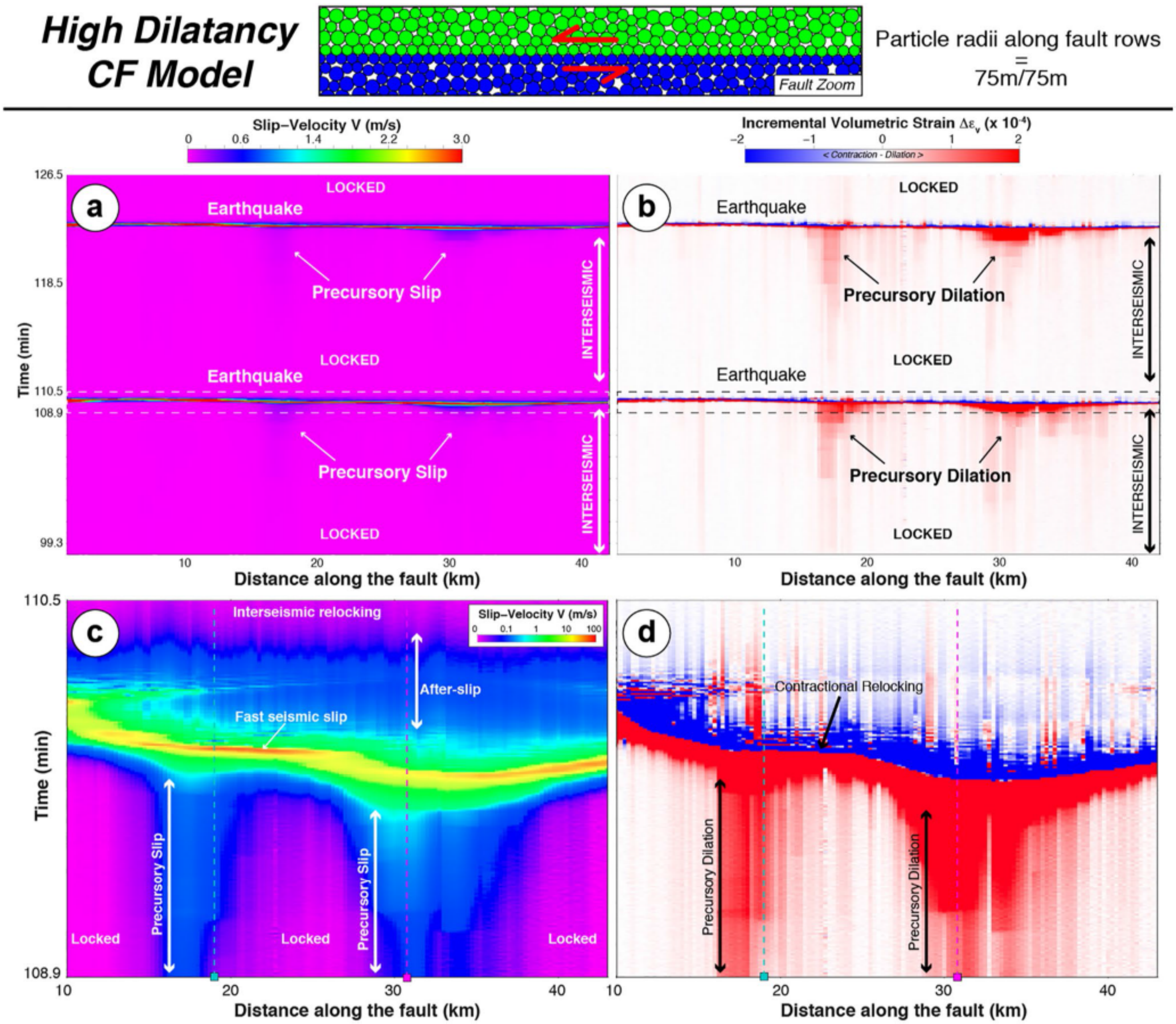

Figure 3. High dilatancy Controlled Fault Model. (a) Time-space maps of the fault slip velocity and (b) related incremental volumetric strain. (c and d) Expanded plots around the fast slip event indicated by the white dashed box in panels (a) and (b), respectively. The slip-velocity color scale is logarithmic to better highlight the range from precursory slow slip to fast earthquakes. Dilation is red, contraction is blue. Data along the vertical dashed lines are detailed in corresponding colored curves of Figure 4.

3.3. Low Dilatancy Controlled Fault Model

The low dilatancy CF Model reveals a very different behavior with the occurrence of slow earthquake sequences and the total absence of earthquakes (Figure 5). The maximum slip velocity V_{max} reaches ~0.6 m/s and the fault is never totally locked even during the quietest periods. The incremental volumetric strain time-space map reveals a very diffuse pattern of low dilational and contractional regions during the quiet period and doesn't clearly show any distinctive dilated zones. During slow earthquakes, the magnitude of volumetric strain is slightly enhanced relative to quieter periods. However, no dynamic acceleration is observed. SEqs are characterized by both contraction and dilation, almost equally expressed along the fault. The strain pattern along such regions of SEq consists of short closely spaced, alternating dilated and contracted areas (see the enlarged inset on Figure 5). This really differs from the large and high-dilation precursors that develop before the onset of dynamic seismic slip generated by the high dilatancy CF Model.

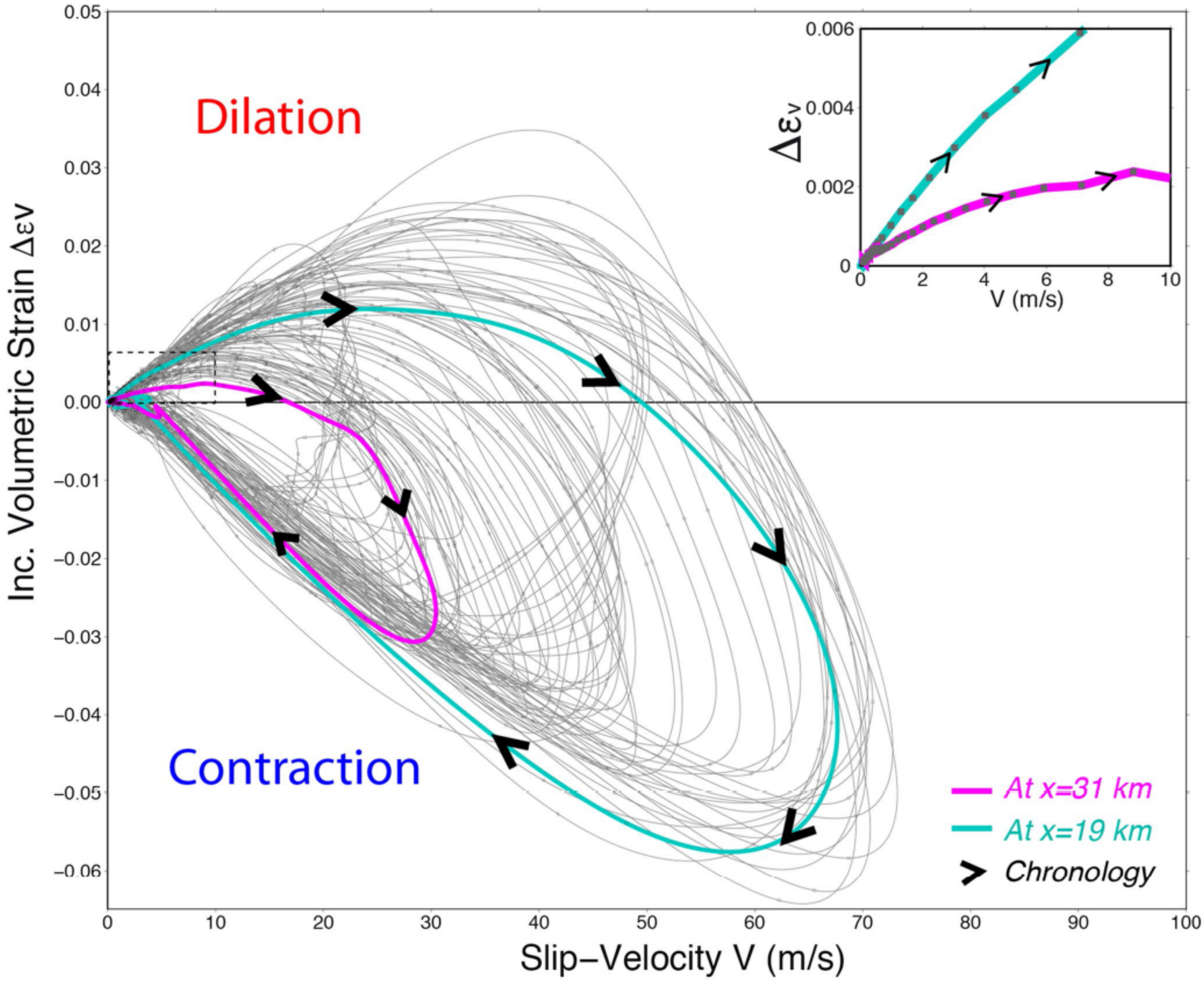

Figure 4. Evolution of the relationship between incremental volumetric strain and slip-velocity along the fault during the sequence detailed in time-space maps of Figures 3c and 3d. Gray curves plot data along all columns of the time-space maps. Blue-green and purple curves highlight the evolution of this relationship at $x = 19$ and 31 km, respectively. The dashed black rectangle delimits the plotted zoom of the upper-right inset.

3.4. Comparative Stress and Dilation Patterns of Controlled Fault Models

Figure 6 compares the evolution of the system stress ratio (τ/σ_n) and dilatancy ($\delta y/\delta x$) with displacement recorded at the walls for three examples of CF Model: the two extreme cases presented above, as well as an intermediate one.

The stress-displacement plot for the high dilatancy CF Model (Figure 6a, dashed red curve) reveals a periodic stick-slip cycle characterized by distinct linear increase in stress ratio followed by a rapid drop in stress ratio, from ~0.64 to 0.39, that coincides with rapid fault slip. Note that this interval ranges above the assigned interparticle friction coefficient value ($\mu_p = 0.2$). Wall displacements ($\delta y/\delta x$) during this sequence (thick red curve) reveal that before each main rupture, the system experiences precursory linear rate of dilation until around 80% of the total interseismic loading. Dilation rate then becomes exponential until the onset of the stress drop and the resulting contraction.

For the low dilatancy model, the stress ratio increases and decreases more gradually, presenting a more symmetric oscillating pattern of loading and unloading (Figure 6c, dashed purple curve). Stress oscillations range between 0.20 and 0.23, very close to the assigned interparticle friction coefficient value of 0.2.

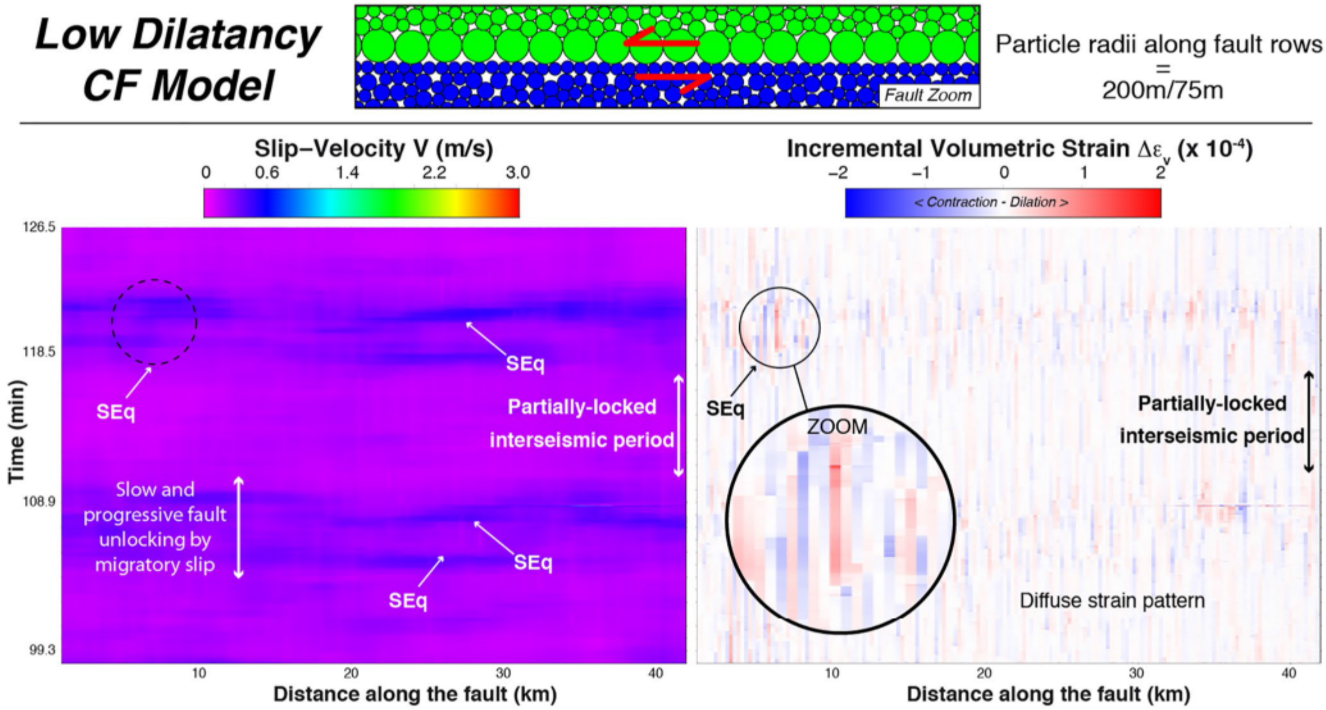

Figure 5. Low dilatancy Controlled Fault Model. Time-space maps of the fault slip velocity (left) and related incremental volumetric strain (right). Dilation is red, contraction is blue. SEq = Slow Earthquake.

Corresponding cycles of very slight system dilation and contraction can be observed (thick purple curve), although there is no clear precursory dilation before the stress-drops.

The intermediate dilatancy CF Model (Figure 6b, green curves) confirms the evidence for the first order role of fault roughness on fault strength and slip behavior. This model reveals an intermediate rate of stress accumulation, followed by a broad peak and intermediate rate and magnitude of stress drop. Similarly, the corresponding dilation and contraction stages are intermediate. Thus, in the controlled fault models, greater fault dilation corresponds to steeper and higher magnitude stress increases, and more dramatic rapid stress drops during contraction.

3.5. Dilation Patterns in the Random Interface Model

The results of the three homogeneous CF Models clearly demonstrate three things: (a) the magnitudes of fault dilation and contraction correlate with the magnitudes of stress increases and drops; (b) the dilatancy of a fault influences the predominant fault slip rate; and (c) fault dilatancy contributes to absolute fault strength. Examining the extremes presented here, we see that high dilatancy results in classic stick-slip frictional behavior characterized by a steady build-up of stress accompanied by dilation, followed by a rapid stress drop and rapid contraction. In contrast, low dilatancy results in oscillating slow events along the length of the fault, accompanied by very slight dilation and contraction. These observations suggest that, to first order, differences in dilatancy may explain the occurrence of earthquakes and slow earthquakes on faults elsewhere. To test that assumption, we revisit the more complex RI Model presented earlier.

The range of slip velocities generated by the RI Model includes all the distinct event types produced by each of the CF Models described above, however, the spatiotemporal patterns of slip are much more complex. For example, the character of precursory dilation is not as simple as in the geometrically controlled fault models. We see that fault dilation occurs in regions of future earthquakes, but it also occurs in association with isolated slow earthquakes. Moreover, in contrast to the more uniform CF Models, the behavior of the fault varies along its length, with adjoining regions exhibiting concurrent dilation and contraction. This pattern makes it difficult to recognize clear relationships between dilation and subsequent slip velocity. Processes

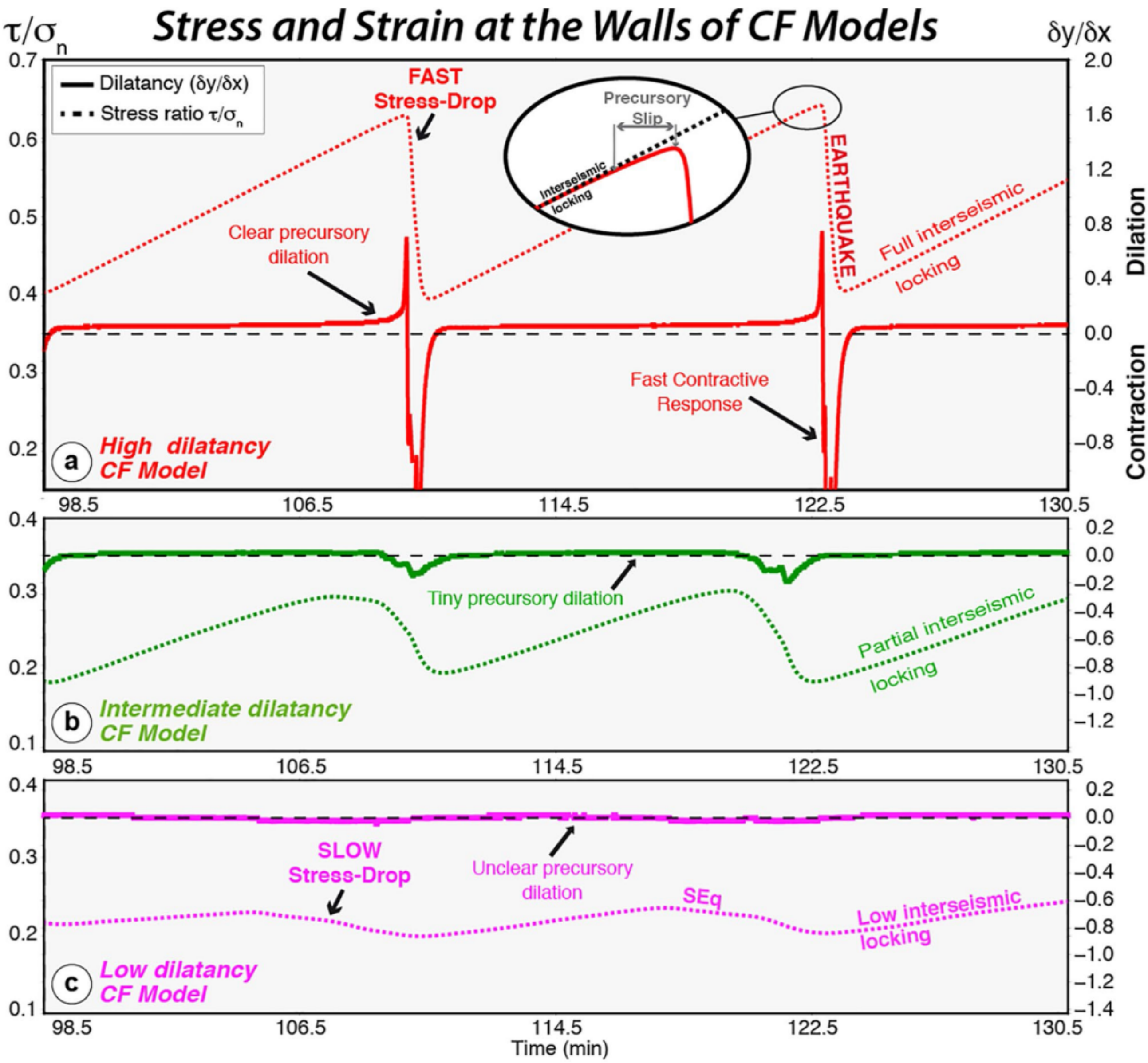

Figure 6. Stress ratios (τ/σ_n) and associated contraction/dilation ($\delta y/\delta x$) patterns of three Controlled Fault (CF) Models system measured at the walls. SEq = Slow Earthquake Event. (a) High dilatancy CF Model (red), with fault particle radii of 75 m/75 m. (b) Intermediate dilatancy CF Model (green), with fault particle radii of 100 m/75 m. (c) Low dilatancy CF Model (purple), with fault particle radii of 200 m/75 m.

local to the nucleation points may not be predictive of the subsequent slip behavior. Thus, it is necessary to evaluate the volumetric strain patterns across the broader slip zones to determine if they correlate with different categories of events.

Incremental volumetric strain patterns along the fault for several examples of events are shown in Figures 7a and 7b, including an isolated slow earthquake (SEq1), several fast earthquakes (Eq1, Eq3, and Eq4), and an intermediate case (Eq2). Profiles of $\Delta\varepsilon_v$ along the fault have been selected to highlight the strain patterns of all these events during their initiation phase (Figures 7c–7f). These profiles have been picked as early as possible before the velocity peak so that the signal is clear enough to be interpreted. Although the rate of strain continues to evolve during the nucleation phases of events, the general patterns remain consistent until the dynamic acceleration period.

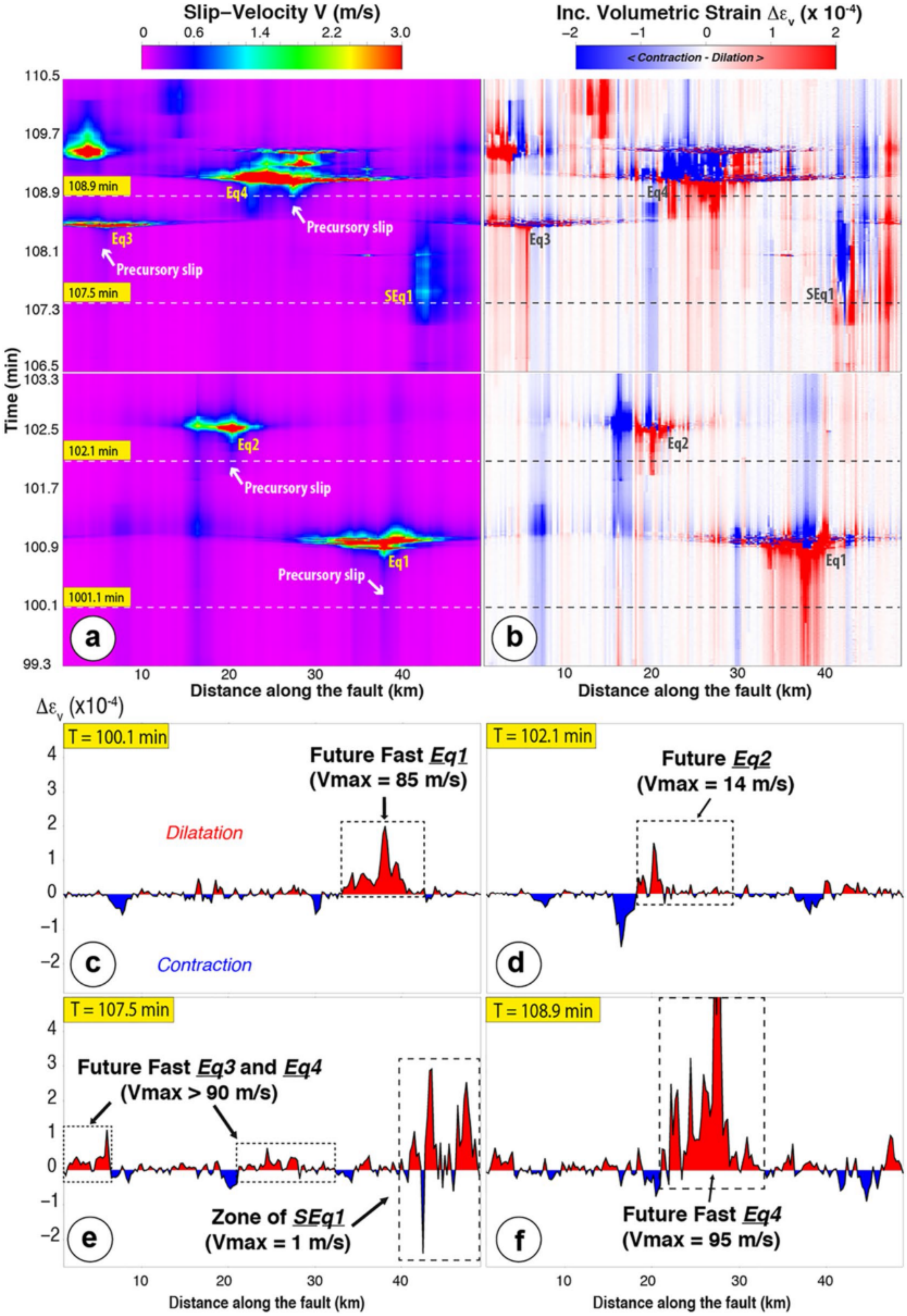

Figure 7. Relationships between precursory incremental volumetric strain patterns and slip-velocity in the rough interface model. The sequences presented here are representative of various types of slip-events. (a) Time-space maps of fault slip-velocity and (b) the corresponding incremental volumetric strain along the fault. Dilation is red, and contraction is blue. Panel (c) through panel (f) along-fault profiles of volumetric strain during precursory stages of various slip-event types, sampled along horizontal black dashed lines in panel (b). Eq = Earthquake; SEq = Slow Earthquake.

The preparation zones of fast earthquakes stand out, as they exhibit wide and anomalously high dilational zones (>15 km length) bounded by very low contractional regions (Figures 7c and 7f). These local strain patterns, which correspond to precursory SSE regions, are comparable to those observed for the high dilatancy CF Model. In contrast, the zone of the isolated SEq1 reveals a more complex volumetric strain distribution (Figure 7e). This region is mostly dilational, however, it also contains several narrow but pronounced contractional features, which alternate with the dilated areas. This alternating pattern is similar to that displayed in the low dilatancy CF Model, although the intensity of strain is significantly higher here, consistent with the greater relief on the fault. Event Eq2 illustrates the precursory strain pattern of an intermediate case that produces moderate slip velocity (Figure 7d). Its preparation zone consists of a wide dilated region of lower magnitude than observed for the other earthquakes, and is bounded by one pronounced contractional zone at its left tip and an almost neutral region at the right tip.

In summary, the few representative examples of preparatory strain evolution prior to fault slip events reveal striking differences between different types of events. Differences in the strain patterns are also evident between single SEq and precursory slow-slip of fast and slower earthquakes. In the following section, we discuss the relationships between fault dilatancy and fault slip stability, and suggest a possible way to distinguish the observed trends.

4. Discussion

4.1. First Order Role of Fault Dilatancy on Slip Behavior and Earthquake Nucleation

The CF Models clearly reveal the first order effect of fault dilatancy on frictional behavior. The more dilatant the fault, the more unstable the fault slip dynamics. In these simple CF models, isolated slow earthquakes occur along low magnitude dilational surfaces that experience minimal change in volume during shearing, characterized by alternating dilational and contractional zones. Conversely, precursory slow-slip leading up to fast seismogenic events is generated along more dilated surfaces, and corresponds to high precursory dilation. At the system scale, the greater the precursory dilation, the faster and larger the coseismic stress drops are that accompany the subsequent fault slip. Such relationships between fault dilation and slip velocity is also evident in the more complex and realistic RI Model, but occur at much more local scales. This demonstrates that the same processes are at play in both types of models.

Consistent with the observations of Blank and Morgan (2019), using a subduction megathrust DEM model setup, earthquake nucleation is preceded by persistent dilation, which is related to the gradual unlocking of an asperity before the dramatic slip acceleration that accompanies the contractive response during the fault relocking. This process results in local fault strength changes as geometrical protrusions ride up and over each other. The precursory process initially is manifest by slow slip, because the asperity resists fault slip until the asperity apex is reached. At that point, the resistance to slip vanishes, allowing rapid slip that overcomes the geometric asperity, enabling the collapse of dilated pore spaces and local contraction, which contribute to fault relocking. Although the peak slip rate is achieved during the contractional stage, seismic slip velocities are achieved during the precursory dilational stage before the onset of fault relocking (Figure 4). This correspondence implies that fault dilation causes gradual slip-weakening and thus instability. This response can be explained by the gradual decrease of the contacting area between protrusions during fault dilation that promotes a reduction in fault strength, leading up to slip acceleration (Beeler et al., 2012).

4.2. Differences Between Precursory Slow-Slip of Earthquakes and Isolated SEq

Blank and Morgan (2019) speculated that slow slip that does not turn into an earthquake is probably related to low relief fault roughness, which minimizes the amount of fault dilation and subsequent contraction of the system. This is confirmed and further demonstrated here with the simple CF Models. However, in the RI Model setup, the more complex geometry of the fault surface leads to a more complex volumetric strain pattern in time and space, as demonstrated in Figure 7. Interestingly, the differences between the various event types are best revealed in meso-scale strain patterns over the lengths of the slip zones, that is, over several kilometers, rather than at the system scale. In the absence of damage within the wall rocks, these strain patterns are primarily related to geometrical characteristics of the fault section of interest. Two contrasting examples are highlighted in Figure 8, which illustrates the geometrical differences between a fault section

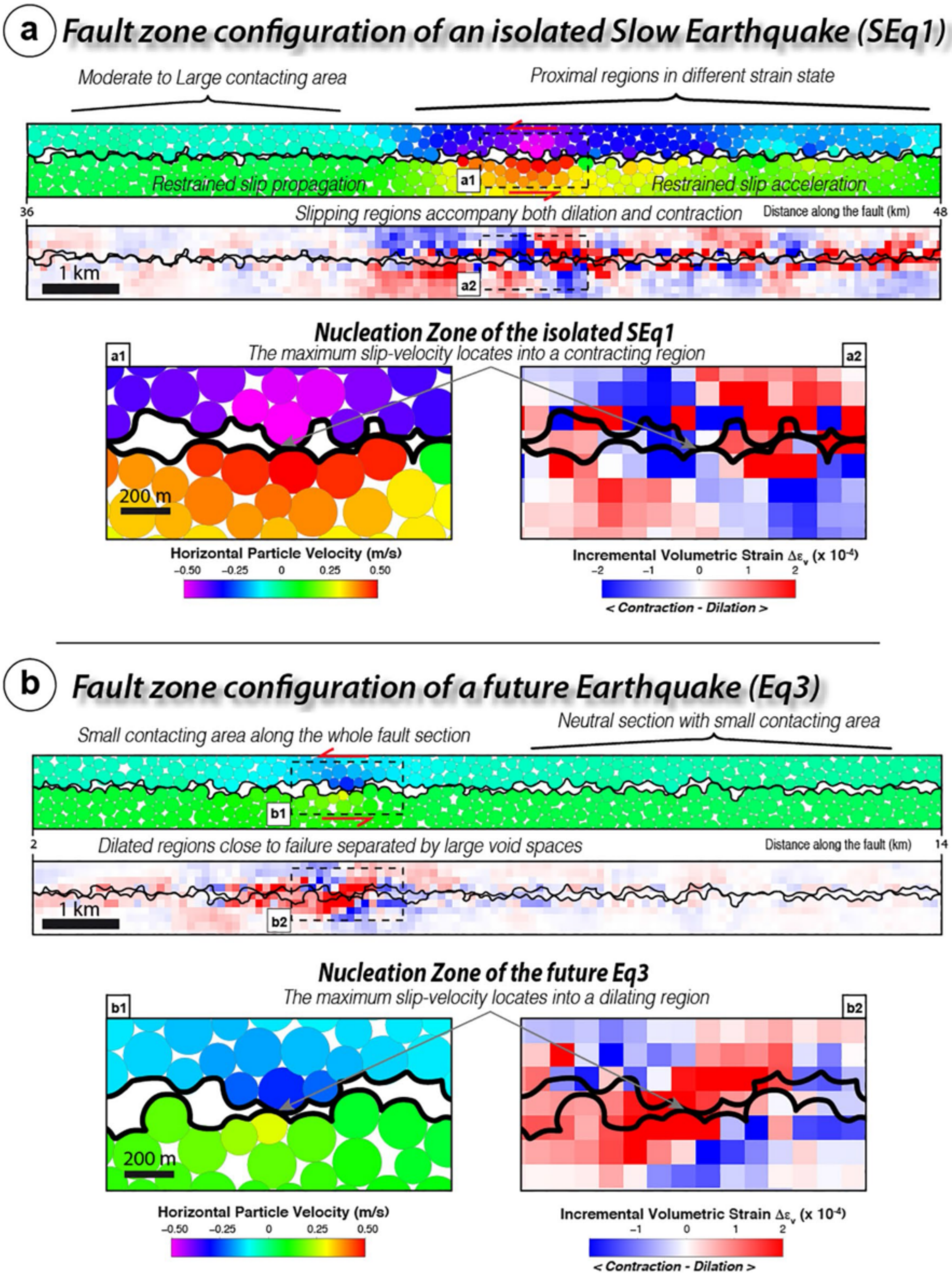

Figure 8. (a) Examples of fault section geometrical configuration along two regions of the rough interface model during the occurrence of the (a) isolated slow earthquake SEq1 and (b) the precursory slow-slip of the earthquake Eq3. The fault sections are mapped out at 107.3 and 108.5 min, respectively. The horizontal particle velocities and the incremental volumetric strain field are superimposed to the mapped fault zone. This allows direct visualization of dilation/contraction patterns revealed by the plotted profiles in Figure 7 and their relationships with the fault slip behavior.

that hosts a slow earthquake (SEq1) and one that generates a fast earthquake (Eq3). To better clarify the relationships among parameters, the horizontal particle velocities and the incremental volumetric strain field are superimposed on the mapped fault zone. This allows direct visualization of the dilation-contraction patterns revealed in the profiles plotted in Figure 7, and their relationships with fault slip behavior. The two anomalous dilating regions of the SEq1 event and of the precursory slow slip for Eq3 are visible on the same profile at 107.5 min (Figure 7e), however, here we picked the precursory Eq3 event features slightly later, at 108.5 min, to better highlight the ongoing slow-slip and associated strain before the dynamic stage. As shown in Figure 8a, the nucleation zone of the SEq1 event exhibits several areas close to their failure points (apex) at different states that accommodate both fault dilation and contraction in response to the far field imposed displacement. Although dilation dominates along this section, the maximum-slip velocity of the SEq1 event occurs in a highly contracting region. Referring back to the correlated trajectories of $\Delta\varepsilon_v$ and V in Figure 4, this suggests that the slow earthquake is not expected to accelerate dramatically, as the slip velocity likely has already reached its peak, or at least is close.

Thus, fault stability depends on the distribution of asperity behaviors prior to slip. If most asperities approach their apexes concurrently (Figure 8b), and are separated by large void spaces, failure can be rapid and unstable (Eq3). In this case, the combination of a small area of contact and the synchronized state of asperities approaching failure through general dilation yields conditions that favor slip acceleration and dynamic slip. However, if intervening asperities are contracting, and if their spacing is close, slip will be slowed due to the added resistance which acts against the general fault lips opening (SEq1, Figure 8a). Movies S2 and S3 in Supporting Information S1 (Caniven et al., 2021 show the detailed evolution of particle displacements across the regions of this two events. Additional analyses of relationships between fault geometry, dilatancy, and slip-velocity are provided for other examples in Supporting Information S1 (Figures S1–S3).

4.3. Implications for Earthquake Energy Balance

An important result that emerges from this study is that, as fault dilation appears as the controlling factor for the slip stability, it must also influence the earthquake energy budget. As the fault dilates, the fault zone is doing work against the applied normal stress; it is also accumulating elastic strain energy through the deformation of asperities and the surrounding rock. This energy will be released during fault slip and contraction, and the magnitude, rate and mode of release will determine the mode of slip. The strain energy consists of dilatational energy due to the change in volume, and distortional energy related to change in shape (Autores, 2006). At the crustal scale, Doglioni et al. (2015) also argued that the so-called "earthquake energy" could be related mostly to the deformed volume around the rupture zone where elastic strain energy is stored during the interseismic stage. This is referred to as the "earthquake volume" (Bath & Duda, 1964), that depends on the local volumetric strain pattern revealed here. This is fully consistent with our results.

Thus, in light of our observations, we can define several key parameters characterizing the strain pattern of regions that experience slow-slip initiation (Figure 9a) to define the energy budget and so the upcoming slip behavior. Figure 9a defines these parameters for a schematic incremental volumetric strain profile along a fault. In this example, the right part of the fault experiences anomalously high dilation. This dilated region can be defined by length L_d, which is bounded by neutral or contractional peaks at its boundaries. We then consider the maximum value of the dilational strain $D_{\max}$ measured along L_d and the value of the maximum contractional strain $C_{\max\text{-}1}$ and $C_{\max\text{-}2}$ at each of the boundaries. Each boundary of the dilated zone can be then defined by a ratio $D_{\max}/C_{\max\text{-}1,2}$.

Basically, conditions for slip acceleration require that the total work, W, done during the stress drop be higher than the dissipated energy E_d along the nucleation region (Beeler, 2007). In a conceptual friction-displacement plot associated with a slip event (Figure 9b), W corresponds to the total area under the system unloading stress curve (stiffness K). E_d, which includes both shear-fracture energy (Griffith, 1921) and energy dissipated by frictional heating (Kanamori & Rivera, 2006) corresponds to the area under the measured friction-drop path. The difference between W and E_d reflects the available energy E_a for slip acceleration, potentially released as seismic energy. In our model, we note that in the absence of temperature changes and new fracture generation, E_d results only from the energy dissipated by frictional sliding.

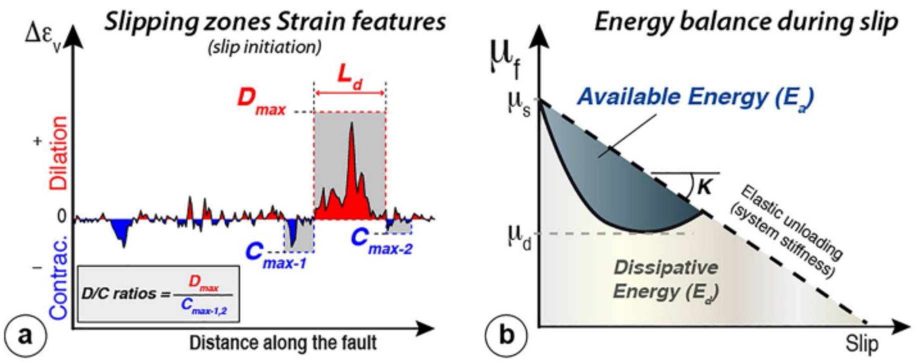

Figure 9. (a) Schematic definition of key parameters through a generic precursory strain pattern. (b) Definition of the fault slip energy balance from the theoretical friction evolution in average over the fault area. The black thick curve indicates the expected friction evolution μ_f with slip during instability and the black thick dashed line indicate the system stiffness K. μ_s and μ_d indicate static and dynamic friction, respectively.

Figure 10 schematically summarizes the relationships among the shear-induced precursory fault dilation along the slipping zone, the energy budget, and the expected slip-behavior response. Diagrammed are four configurations, corresponding to different degrees of relative dilation (increasing from left to right, referred to as columns 1–4), along with the hypothesized strength versus slip behavior. According to our results, the region with the fastest slip events ($V_{\max} > 10$ m/s) in the model would exhibit a large dilated zone (Figure 10, column 4) with $L_d > \sim 10$ km, bounded by very low contractional or neutral regions, resulting in high $D_{\max}/C_{\max}$ ratios (>>1). The amount of dilation along this portion of the fault is much higher than the amount of

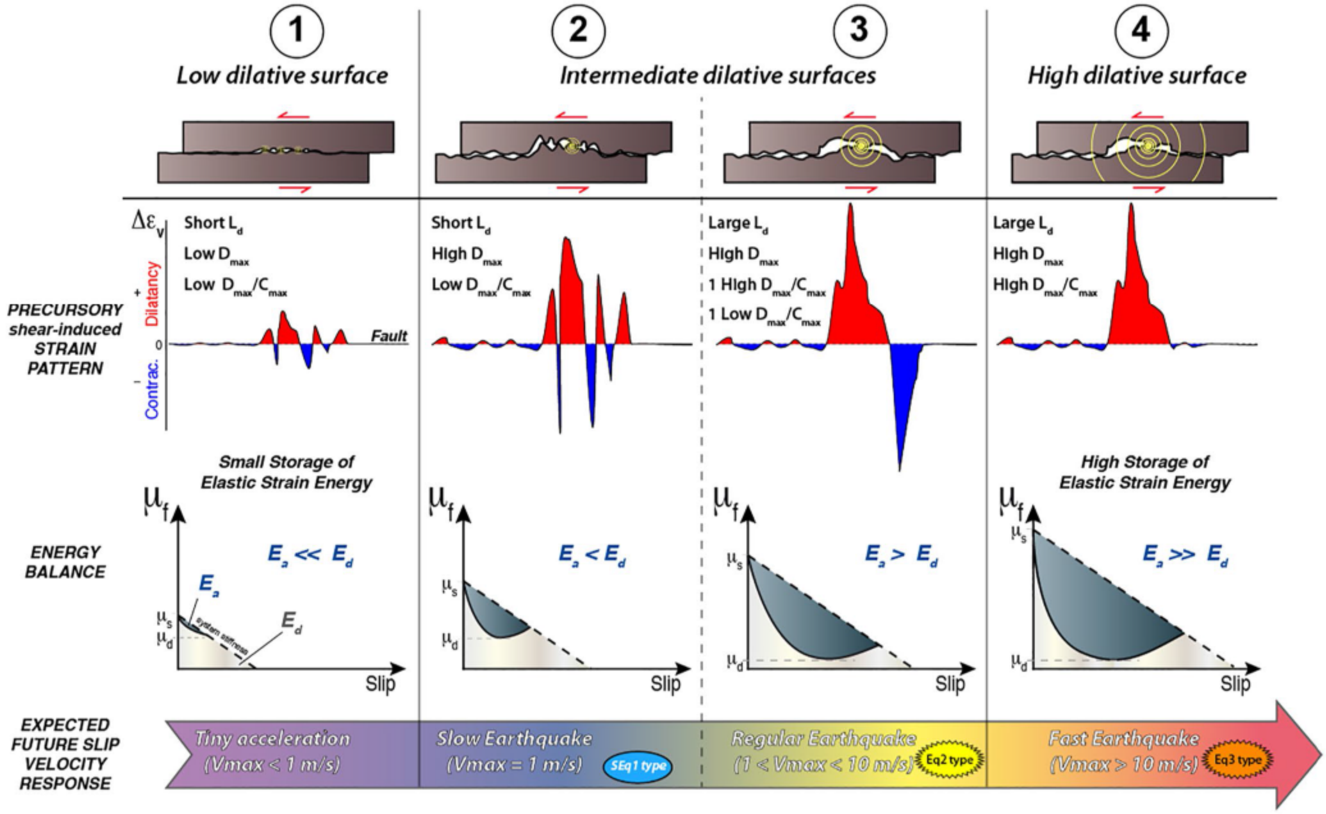

Figure 10. Relationships between precursory fault dilatancy through the slipping zone, energy budget, and expected slip-behavior response. The black thick curve in energy balance plots indicates the expected friction evolution μ_f with slip during instability and the dashed line indicate the system stiffness K. Yellow concentric circles along the fault surfaces (top) indicate the main nucleation points and the expected seismic wave radiation of events.

contraction, allowing a high amount of elastic strain energy to be stored (e.g., Eq3 event). Because of the decrease in contacting area, high dilation leads to the earthquake through a dramatic reduction in fault strength, causing stress-drop to be faster than the general elastic relaxation of the system (related to stiffness K). It implies that minimal work is spent during the precursory slip phase and most of the elastic strain energy is stored around the expanding fault zone. Thus, for regions of the fault with high dilation, shear fracture energy and frictional heat dissipation would be minimized (Rowe, 1962), promoting efficient storage of dilational strain as seismic energy available to radiate.

In contrast, for the slowest slip events ($V_{max} < 1$ m/s), the preparation zone consists of several narrow, closely spaced, small magnitude dilational regions ($L_d < \sim 5$ km) separated by contractional domains (Figure 10, column 1). Most of the D_{max}/C_{max} ratios along this section are low, close to 1. These slower-slip events, approaching the imposed far-field velocity loading rate (or less), occur in low relief regions. Under these conditions, the contribution of contracting fault regions is much lower than for the slightly faster events such as SEq1. Indeed, the fault strength of such low relief zones is weak, largely because the fault doesn't require pronounced dilation to slip. As a consequence, the static friction tends to approach the sliding friction (or the assigned interparticle friction) value in our model (Figure 6c). Under these conditions, most asperities along such sections tend to slip together, without significant resistance. As the fault line exhibits, however, some slight topographic variations, that is, sliding asperities, promote fault dilation while others accommodate contraction, providing a diffuse and oscillating strain pattern. In such slow-slip regions, the maximum slip velocity occurs earlier in the contractional areas, where the resistance locally vanishes. This results in the dissipation of the strain energy mostly through slow aseismic slip. Indeed, as the fault strength is low, more energy is dissipated by slip on existing surfaces, and less work is needed to accommodate the far-field loading. Under these conditions, E_d tends to approach W, and E_a is considerably reduced. A similar configuration with higher fault relief (Figure 10, column 2) would enable slightly faster slow-slip events ($V_{max} \sim 1$ m/s) (e.g., SEq1 event), where dynamic slip acceleration is moderately restrained by the presence of contractional asperities into the mostly dilated region. The third case (Figure 10, column 3) recall the configuration of the fastest slip case (Figure 10, column 4) but with the presence of a strong contractional asperity at one tip of the dilated region that tends to resist slip acceleration ($1 < V_{max} < 10$ m/s) during the dynamic stage (e.g., Eq2 event, see Figure S2 in Supporting Information S1).

We recognize that our energy budget is also affected by damping used here and maybe by other not explored numerical parameters. Nevertheless, we believe that the relative changes that we see and the first-order controls on these can be attributed to fault roughness. Although more work could be done in the future to quantify more rigorously the energy budget, our point, therefore, is that first-order controls that we recognize likely play a role in nature as well.

4.4. Control on Normal Stress and Nucleation Size in the Rate-and-State Framework

We note that, to first order, the relationship between fault dilatancy and slip stability is similar to what has been observed experimentally with changes in normal stress on a spring-slider system (Baumberger et al., 1999; Scholz, 2002). In that case, decreases in normal load lead to a transition from stick-slip to stable sliding, passing through a minor domain of oscillatory motion near the stability limit. In our case, the normal load applied to the boundaries of the system is maintained at a constant value by a servo-controlled mechanism that simulates lithostatic confinement. Nonetheless, our faults experience local changes in normal stress, contributing to a heterogeneous distribution of fault strength (i.e., resisting force) with slip, due to local locking and release along geometric asperities. The mechanism proposed here is consistent with the "asperities on asperity" concept formulated by Archard (1961, 1958). Indeed, based on experimental results, it is shown that normal stress field variations along local contact asperities are indicative of local variations in shear strength along the region of interest (Nayak, 1973; Yoshioka & Scholz, 1989). Theoretical work using continuum mechanics by Romanet et al. (2020) show that the main effect of geometrical features is to change the normal traction along the fault, the local curvature of the fault being enhanced by the shear slip. This suggests a direct correspondence between normal traction and contraction/dilatation. Based on 2-D quasi-dynamic elastic simulations of rate-state faults, Cattania and Segall (2021) also explained a broad range of fault slip behavior by normal traction variations due to complex geometry.

With regards to the rate-and-state friction laws (Scholz, 1998), derivations from elastodynamics (Rubin & Ampuero, 2005) imply that the higher the effective normal stress, the shorter the critical nucleation length L_c of the slipping region above which instability occurs. In our model, this implies that the amount of fault dilation that precedes slip controls L_c via the local effective normal stress changes along asperities. Dynamic instability is favored by a highly dilated fault that induces high local compressive normal stresses and small L_c (see normal stress and slip distributions of Fournier and Morgan (2012)). Conversely, stable slip is favored by a minimally dilated fault which distributes the compressive normal stresses across more asperities, and larger effective L_c.

4.5. Comparisons With Previous Investigations of Geometrical Effects

A concluding remark from this study is that a slow-slip can turn into either an earthquake or an isolated slow earthquake depending on (a) the amount of shear-induced dilation, (b) the dilation/contraction ratio for each of the dilated region boundaries, (c) the proximity of the asperities to their respective failure points, and (d) the spacing between the asperities in the potential failure zone. This latter parameter also has been considered by previous studies. Several studies have demonstrated that elastic interactions may affect local variations in fault stiffness because of the density and spacing of local asperities (Braun et al., 2012; Braun & Peyrard, 2012; Campañá et al., 2011; Ciavarella et al., 2008). The separation distance λ between the asperities is proposed as a key parameter controlling their potential elastic interaction and the resulting fault slip-stability. Based on their experimental results, Harbord et al. (2017) proposed that the condition $\lambda > L_c$ must be satisfied for an instability that turns into a dynamic slip event. This suggests that for two given fault regions with similar amounts of incremental dilation (a proxy for normal stress changes), the one consisting of multiple closely spaced asperities will tend to slip more slowly because λ tends to be closer to L_c. This is illustrated in our model by both the mostly dilated region of the SEq1 event and of the preparing Eq3 event area exhibiting short and large separating distances, respectively. We suggest that this relationship also can be explained by the fact that an increase in the density of asperities reduces the probability that all of them are similarly close to their failure condition, thus reducing the likelihood of unstable slip acceleration.

4.6. Model Limitations and Capabilities

As for any model, certain approximations and simplifications are employed in order to examine specific phenomena. Our simplified model set-up and necessary boundary conditions introduce certain limitations in the application of our results to natural processes, as summarized here.

One of the discrepancies recognized between our model and natural fault systems is the difference in magnitudes of the output slip-velocities. Our "slow earthquakes" exhibit slip rates on the order of 0.1 m/s, which, although slower than the common earthquake threshold of 1 m/s, still correspond to the upper limit of typical slow earthquakes, for example, with slip-velocities on the order of centimeters per day to years. Furthermore, the maximum slip-rate of our earthquakes ranges on the order of 10–100 m/s, somewhat faster than the more common earthquake slip velocity inferred as ~1 m/s. A first observation to make is that our velocities are measured as instantaneous slip rates immediately adjacent to the fault, in contrast field-based earthquake slip rates, which are averaged over both space and time, and thus likely underestimated. Nonetheless, there are several numerical factors that likely play a role, in particular, model loading rate and particle size.

Loading rate is a critical parameter that may cause time-scaling distortion when it differs from natural rates. As a consequence, the time scaling problem is a common issue for both numerical and experimental approaches. At the higher end of our slip values, our DEM simulations yield geologically reasonable slip rates (on the order of m/s) as long as the material properties are similar to natural systems (Blank & Morgan, 2019). However, the lower part of the slip-velocity spectrum can be affected by distortions due to the necessary high loading rates compared to the real tectonic rate. This is similar to challenges present during rock deformation experiments or analog models. One of the consequences of such distortion is the compression of the interseismic time-scale, pushing the slowest slip events to velocities closer to fast earthquakes. In our numerical simulations using a relatively high loading rate value of 0.2 m/s suggests that we should define continuous creep as equal to or lower than 0.2 m/s, transient slow slip between 0.2 m/s and the classic earthquake threshold value of 1 m/s, and fast earthquakes above ~1 m/s (Di Toro et al., 2004). These definitions are consistent with previous DEM works using this code (Blank & Morgan, 2019; Blank et al., 2021; Fournier & Morgan, 2012).

Particle size can play a critical role in the slip behavior. As illustrated by Fournier and Morgan (2012) with the same code (Ricebal), smaller particles result in reduced fault resistance, and lower magnitudes of coseismic slip. Even the larger particles that we use in our study show that fault roughness is a key controlling factor, even as we recognize that the larger particle sizes used exaggerates this control, for example, reducing the potential to generate isolated very slow slip in our models. In addition, due to restricted bond breakage, fault roughness cannot evolve, for example, by fault damage fault segmentation and asperity smoothing. As a consequence, we expect that our high fault roughness and high strength probably slightly shift the natural range of slip velocities toward higher values relative to natural systems, explaining in part both our "fast" slow earthquakes and even faster earthquakes.

The lack of fluid and temperature gradients in our models may also contribute to these discrepancies. Indeed, although fluid-pressure is expected to work in tandem with dilatancy in our model (negative pore pressure would accompany precursory dilation and slow-slip whereas collapsing pores would lead to over-pressurization during the dynamic final contraction) (Blank & Morgan, 2019), thermal-pressurization has been suggested as a competing mechanism against dilatancy (Segall & Bradley, 2012; Sinha et al., 2019) that could dampen the fast motions produced in our model.

Nevertheless, despite of these discrepancies in absolute slip-velocity values, we believe that the processes revealed here provide important insights into the simple geometric controls on relative slip velocities that likely apply across the entire spectrum of fault slip. Although our loading rate (0.2 m/s) is fast, it is numerically beneficial, ensuring reasonable simulation times, and the opportunity to examine numerous seismic cycles over a short period of time, during which a broad range of slip behavior can be investigated.

4.7. Implication for Natural Systems

Results of the RI Models show that the system dilatancy measured at the boundaries does not directly correlate with the evolution in fault slip velocity (Figure 2d), in contrast to the results of the simpler CF Models. This is because the complex volumetric strain "bar code" that evolves through time and space along the fault zone of the RI Model is averaged and smoothed at the system scale. The critical controls that govern fault slip behavior occur locally along the fault itself. This partially explains why the search for evidence of dilation-related precursors from geophysical data in natural systems has largely failed (Main et al., 2012); we are not observing fault processes at the necessary scale. This also reinforces the need to look more closely immediately adjacent to the fault zone, although it would be difficult to achieve the local spatial coverage necessary to resolve the dilational patterns. However, recent technical developments such as the seismic interferometry or "passive ballistic wave monitoring" using a dense array could help to achieve this goal. The method is theoretically based on the detection of the expected seismic velocity changes in the vicinity of moving faults at seismogenic depths around the nucleation zones of earthquakes. This requires continuously operating high-energy seismic sources, possible provided by human activities such as vehicle traffic. Based on this approach, Brenguier et al. (2019) for example, successfully used heavy freight trains as powerful repetitive seismic source to continuously probe the San Jacinto fault (California) down to 4 km depth along a 50 km long section.

Our results show that the volumetric strain pattern around the fault zone itself appears to be a good proxy for the geometrical complexity of the fault and its potential control on slip behavior. This is consistent with numerous studies that highlight the critical role of the internal structure of faults and especially the roughness of slipping surfaces on frictional behavior (Renard & Candela, 2017; Tal et al., 2018; Wibberley, 2008; Zielke et al., 2017). Our study demonstrates that the volumetric strain pattern is potentially predictive when densely measured at the fault zone (e.g., every few 100 m in this study) along several kilometer sections. Conversely, as stated by investigations of precursory signal of natural earthquakes (Amoruso & Crescentini, 2010) as well as dislocation model testing (Abercrombie et al., 1995), measurements too far from the fault plane (i.e., from geodesy) or too isolated (e.g., in boreholes) may not capture the strain pattern with high enough resolution to assess future slip behavior. This is illustrated here in this study as distinct locally high dilation, that is, along regions <1 km length, which do not indicate nucleation regions of dynamic events systematically. For example, we see high dilation peaks in regions of both future earthquakes and slower slip events as for the SEq1 event (Figure 7e). This could have significant implications for earthquake forecasting methods and new technical developments of monitoring systems (Lee & Wu, 2009; Tehseen et al., 2020). In this way, tracking and monitoring ongoing slow earthquakes appears to be critical to better assess seismic hazard.

5. Conclusion

Fault dilation is revealed to be a key factor controlling fault slip stability. At first order, results reveal that the more dilative the fault interface, the more unstable the fault dynamics. Fault slip accelerates during fault dilation, reaching peak velocity during fault contraction whereas slow earthquakes are preceded by minimal dilation, or no change in volume. We also demonstrate that the specific patterns of fault zone dilation and contraction can explain a wide range of slip velocities, from creep to fast earthquakes. The spatio-temporal distribution of dilative and contractive regions along the fault at a given stage proves to correlate with the future slip-velocity evolution, which can be explained by the effects on the earthquake energy budget. This has broader implications as well, in particular, suggesting that slow earthquakes that initiate in large dilated regions bounded by neutral or low contractional areas might turn into earthquakes, whereas the ones occurring in regions dominated by low dilation alternating with contractional asperities tend not to accelerate and may simply stop as isolated slow events. Fault dilation appears, to relate directly to slip stability. This study reinforces our convictions about the existence of strain precursors and highlights the importance of making measurements of evolving properties as close as possible to the fault zone.

Data Availability Statement

All datasets and material underlying this study are published open access in Caniven et al. (2021) (https://doi.org/10.5281/zenodo.4714666) and additional details are provided in Supporting Information S1.

Acknowledgments
This work was funded by the Earth, Environmental & Planetary Science Department of Rice University, National Science Foundation grant EAR–1723249, the Agence Nationale de la Recherche grant ANR-18-CE01-0017 (Topo-Extreme), and support from the Rice University Department of Earth, Environmental, and Planetary Sciences. The authors thank Rodolphe Cattin for supporting part of postdoctoral fellowships grants in the project. Computing facilities were made available in part through the Rice Center for Computational Geophysics. The authors thank the editor Rachel Abercrombie, Pierre Romanet, an anonymous reviewer and the associate editor, for their useful reviews.

References

Abercrombie, R. E., Agnew, D. C., & Wyatt, F. K. (1995). Testing a model of earthquake nucleation. *Bulletin of the Seismological Society of America*, *85*, 1873–1878. https://doi.org/10.1785/bssa0850061873

Abercrombie, R. E., & Ekström, G. (2003). A reassessment of the rupture characteristics of oceanic transform earthquakes. *Journal of Geophysical Research*, *108*. https://doi.org/10.1029/2001JB000814

Amoruso, A., & Crescentini, L. (2010). Limits on earthquake nucleation and other pre-seismic phenomena from continuous strain in the near field of the 2009 L'Aquila earthquake. *Geophysical Research Letters*, *37*, a–n. https://doi.org/10.1029/2010GL043308

Archard, J. F. (1958). *Elastic deformation and the laws of friction*.

Archard, J. F. (1961). Single contacts and multiple encounters. *Journal of Applied Physics*, *32*, 1420–1425. https://doi.org/10.1063/1.1728372

Autores, V. (2006). *Earthquakes: Radiated energy and the physics of faulting*. Wiley.

Barbot, S. (2019). Slow-slip, slow earthquakes, period-two cycles, full and partial ruptures, and deterministic chaos in a single asperity fault. *Tectonophysics*, *768*, 228171. https://doi.org/10.1016/j.tecto.2019.228171

Bath, M., & Duda, S. J. (1964). Earthquake volume, fault plane area, seismic energy, strain, deformation and related quantities. *Annals of Geophysics*, *17*, 353–368. https://doi.org/10.4401/ag-5213

Baumberger, T., Berthoud, P., & Caroli, C. (1999). Physical analysis of the state- and rate-dependent friction law. II. Dynamic friction. *Physical Review B: Condensed Matter*, *60*, 3928–3939. https://doi.org/10.1103/PhysRevB.60.3928

Beeler, N., Kilgore, B., McGarr, A., Fletcher, J., Evans, J., & Baker, S. R. (2012). Observed source parameters for dynamic rupture with non-uniform initial stress and relatively high fracture energy. *Journal of Structural Geology, Physico-Chemical Processes in Seismic Faults*, *38*, 77–89. https://doi.org/10.1016/j.jsg.2011.11.013

Beeler, N. M. (2007). Laboratory-observed faulting in intrinsically and apparently weak materials. In *The seismogenic zone of subduction thrust faults* (p. 80). Columbia University Press.

Bizzarri, A., & Cocco, M. (2006). A thermal pressurization model for the spontaneous dynamic rupture propagation on a three-dimensional fault: 1. Methodological approach. *Journal of Geophysical Research*, *111*. https://doi.org/10.1029/2005JB003862

Blank, D., Morgan, J., & Caniven, Y. (2021). Geometrically controlled slow slip enhanced by seismic waves: A mechanism for delayed triggering. *Earth and Planetary Science Letters*, *554*, 116695. https://doi.org/10.1016/j.epsl.2020.116695

Blank, D. G., & Morgan, J. K. (2019). Precursory stress changes and fault dilation lead to fault rupture: Insights from discrete element simulations. *Geophysical Research Letters*, *46*, 3180–3188. https://doi.org/10.1029/2018GL081007

Braun, O. M., & Peyrard, M. (2012). Crack in the frictional interface as a solitary wave. *Physical Review E - Statistical Physics, Plasmas, Fluids, and Related Interdisciplinary Topics*, *85*, 026111. https://doi.org/10.1103/PhysRevE.85.026111

Braun, O. M., Peyrard, M., Stryzheus, D. V., & Tosatti, E. (2012). Collective effects at frictional interfaces. *Tribology Letters*, *48*, 11–25. https://doi.org/10.1007/s11249-012-9913-z

Brenguier, F., Boué, P., Ben-Zion, Y., Vernon, F., Johnson, C. W., Mordret, A., et al. (2019). Train traffic as a powerful noise source for monitoring active faults with seismic interferometry. *Geophysical Research Letters*, *46*, 9529–9536. https://doi.org/10.1029/2019GL083438

Campañá, C., Persson, B. N. J., & Müser, M. H. (2011). Transverse and normal interfacial stiffness of solids with randomly rough surfaces. *Journal of Physics: Condensed Matter*, *23*, 085001. https://doi.org/10.1088/0953-8984/23/8/085001

Caniven, Y., Dominguez, S., Soliva, R., Peyret, M., Cattin, R., & Maerten, F. (2017). Relationships between along-fault heterogeneous normal stress and fault slip patterns during the seismic cycle: Insights from a strike-slip fault laboratory model. *Earth and Planetary Science Letters*, *480*, 147–157. https://doi.org/10.1016/j.epsl.2017.10.009

Cattania, C., & Segall, P. (2021). Precursory slow slip and foreshocks on rough faults. *Journal of Geophysical Research: Solid Earth*, *126*, e2020JB020430. https://doi.org/10.1029/2020JB020430

Ciavarella, M., Greenwood, J. A., & Paggi, M. (2008). Inclusion of "interaction" in the Greenwood and Williamson contact theory. *Wear*, *265*(5–6), 729–734. https://doi.org/10.1016/j.wear.2008.01.019

Cundall, P. A. (1987). Distinct element models of rock and soil structure. *Analytical and Computational Methods in Engineering Rock Mechanics*, 129–163.

Cundall, P. A., & Strack, O. D. L. (1979). A discrete numerical model for granular assemblies. *Géotechnique*, *29*, 47–65. https://doi.org/10.1680/geot.1979.29.1.47

Dean, S., Morgan, J., & Fournier, T. (2013). Geometries of frontal fold and thrust belts: Insights from discrete element simulations. *Journal of Structural Geology*, *53*, 43–53. https://doi.org/10.1016/j.jsg.2013.05.008

Di Toro, G., Goldsby, D. L., & Tullis, T. E. (2004). Friction falls towards zero in quartz rock as slip velocity approaches seismic rates. *Nature*, *427*, 436–439. https://doi.org/10.1038/nature02249

Doglioni, C., Barba, S., Carminati, E., & Riguzzi, F. (2015). Fault on-off versus strain rate and earthquakes energy. *Geoscience Frontiers*, *6*(2), 265–276. https://doi.org/10.1016/j.gsf.2013.12.007

Ferdowsi, B., Griffa, M., Guyer, R. A., Johnson, P. A., Marone, C., & Carmeliet, J. (2013). Microslips as precursors of large slip events in the stick-slip dynamics of sheared granular layers: A discrete element model analysis. *Geophysical Research Letters*, *40*, 4194–4198. https://doi.org/10.1002/grl.50813

Fournier, T., & Morgan, J. (2012). Insights to slip behavior on rough faults using discrete element modeling. *Geophysical Research Letters*, *39*, a–n. https://doi.org/10.1029/2012GL051899

Frank, F. C. (1965). On dilatancy in relation to seismic sources. *Reviews of Geophysics*, *3*, 485–503. https://doi.org/10.1029/RG003i004p00485

Frank, W. B., Shapiro, N. M., Husker, A. L., Kostoglodov, V., Romanenko, A., & Campillo, M. (2014). Using systematically characterized low-frequency earthquakes as a fault probe in Guerrero, Mexico. *Journal of Geophysical Research: Solid Earth*, *119*, 7686–7700. https://doi.org/10.1002/2014JB011457

Freudenthal, A. M. (1975). Shear dilatancy in rock and precursory changes in seismic velocities. *Geophysical Research Letters*, *2*, 517–520. https://doi.org/10.1029/GL002i011p00517

Gao, K., Euser, B. J., Rougier, E., Guyer, R. A., Lei, Z., Knight, E. E., et al. (2018). Modeling of stick-slip behavior in sheared granular fault gouge using the combined finite-discrete element method. *Journal of Geophysical Research: Solid Earth*, *123*, 5774–5792. https://doi.org/10.1029/2018JB015668

Gomberg, J. (2010). Slow slip phenomena in Cascadia from 2007 and beyond: A review. *GSA Bulletin*, *122*, 963978–978. https://doi.org/10.1130/B30287.1

Griffith, A. A. (1921). The phenomena of rupture and flow in solids. *Philosophical Transactions of the Royal Society of London,Series A*, *221*, 163–198. https://doi.org/10.1098/rsta.1921.0006

Harbord, C. W. A., Nielsen, S. B., Paola, N. D., & Holdsworth, R. E. (2017). Earthquake nucleation on rough faults. *Geology*, *45*, 931–934. https://doi.org/10.1130/G39181.1

Hawthorne, J. C., & Bartlow, N. M. (2018). Observing and modeling the spectrum of a slow slip event. *Journal of Geophysical Research: Solid Earth*, *123*, 4243–4265. https://doi.org/10.1029/2017JB015124

Ide, S., Beroza, G. C., Shelly, D. R., & Uchide, T. (2007). A scaling law for slow earthquakes. *Nature*, *447*, 76–79. https://doi.org/10.1038/nature05780

Kanamori, H., & Rivera, L. (2006). Energy partitioning during an earthquake. In *Earthquakes: Radiated energy and the physics of faulting* (pp. 3–13). American Geophysical Union (AGU). https://doi.org/10.1029/170GM03

Khoshmanesh, M., & Shirzaei, M. (2018). Episodic creep events on the San Andreas Fault caused by pore-pressure variations. *Nature Geoscience*, *11*, 610–614. https://doi.org/10.1038/s41561-018-0160-2

Kirkpatrick, J. D., Fagereng, Å., & Shelly, D. R. (2021). Geological constraints on the mechanisms of slow earthquakes. *Nature Reviews Earth & Environment*, *2*, 285–301. https://doi.org/10.1038/s43017-021-00148-w

Lapusta, N., Rice, J. R., Ben-Zion, Y., & Zheng, G. T. (2000). Elastodynamic analysis for slow tectonic loading with spontaneous rupture episodes on faults with rate- and state-dependent friction. *Journal of Geophysical Research*, *105*, 23765–23789. https://doi.org/10.1029/2000JB900250

Lee, W. H. K., & Wu, Y.-M. (2009). Earthquake monitoring and early warning systems. In R. A. Meyers (Ed.), *Encyclopedia of complexity and systems science* (pp. 2496–2530). Springer. https://doi.org/10.1007/978-0-387-30440-3_152

Leeman, J. R., Saffer, D. M., Scuderi, M. M., & Marone, C. (2016). Laboratory observations of slow earthquakes and the spectrum of tectonic fault slip modes. *Nature Communications*, *7*, ncomms11104. https://doi.org/10.1038/ncomms11104

Lockner, D. A., Morrow, C., Moore, D., & Hickman, S. (2011). Low strength of deep San Andreas fault gouge from SAFOD core. *Nature*, *472*, 82–85. https://doi.org/10.1038/nature09927

Main, I. G., Bell, A. F., Meredith, P. G., Geiger, S., & Touati, S. (2012). The dilatancy–diffusion hypothesis and earthquake predictability. *Geological Society, London, Special Publications*, *367*, 215–230. https://doi.org/10.1144/SP367.15

Mead, W. J. (1925). The geologic role of dilatancy. *The Journal of Geology*, *33*, 685–698. https://doi.org/10.1086/623241

Miller, M. M., Melbourne, T., Johnson, D. J., & Sumner, W. Q. (2002). Periodic slow earthquakes from the Cascadia subduction zone. *Science*, *295*, 2423–2423. https://doi.org/10.1126/science.1071193

Morgan, J. (2015). Effects of cohesion on the structural and mechanical evolution of fold and thrust belts and contractional wedges: Discrete element simulations. *Journal of Geophysical Research: Solid Earth*, *120*, 3870–3896. https://doi.org/10.1002/2014JB011455

Nadeau, R. M., & McEvilly, T. V. (2004). Periodic pulsing of characteristic microearthquakes on the San Andreas Fault. *Science*, *303*, 220–222. https://doi.org/10.1126/science.1090353

Nayak, P. R. (1973). Random process model of rough surfaces in plastic contact. *Wear*, *26*, 305–333. https://doi.org/10.1016/0043-1648(73)90185-3

Nur, A. (1972). Dilatancy, pore fluids, and premonitory variations of ts/tp travel times. *Bulletin of the Seismological Society of America*, *62*, 1217–1222. https://doi.org/10.1785/bssa0620051217

Obara, K., & Kato, A. (2016). Connecting slow earthquakes to huge earthquakes. *Science*, *353*, 253–257. https://doi.org/10.1126/science.aaf1512

Radiguet, M., Cotton, F., Vergnolle, M., Campillo, M., Walpersdorf, A., Cotte, N., & Kostoglodov, V. (2012). Slow slip events and strain accumulation in the Guerrero gap, Mexico. *Journal of Geophysical Research*, *117*. https://doi.org/10.1029/2011JB008801

Renard, F., & Candela, T. (2017). Scaling of fault roughness and implications for earthquake mechanics. In *Fault zone dynamic processes* (pp. 195–215). American Geophysical Union (AGU). https://doi.org/10.1002/9781119156895.ch10

Romanet, P., Bhat, H. S., Jolivet, R., & Madariaga, R. (2018). Fast and slow slip events emerge due to fault geometrical complexity. *Geophysical Research Letters*, *45*, 4809–4819. https://doi.org/10.1029/2018GL077579

Romanet, P., Sato, D. S., & Ando, R. (2020). Curvature, a mechanical link between the geometrical complexities of a fault: Application to bends, kinks and rough faults. *Geophysical Journal International*, *223*, 211–232. https://doi.org/10.1093/gji/ggaa308

Rousset, B., Bürgmann, R., & Campillo, M. (2019). Slow slip events in the roots of the San Andreas fault. *Science Advances*, *5*, eaav3274. https://doi.org/10.1126/sciadv.aav3274

Rowe, P. W. (1962). The stress-dilatancy relation for static equilibrium of an assembly of particles in contact. *Proceedings of the Royal Society of London - Series A: Mathematical and Physical Sciences*, *269*, 500–527. Retrieved from https://www.jstor.org/stable/2414551

Rubin, A. M., & Ampuero, J.-P. (2005). Earthquake nucleation on (aging) rate and state faults. *Journal of Geophysical Research*, *110*. https://doi.org/10.1029/2005JB003686

Ruiz, S., Metois, M., Fuenzalida, A., Ruiz, J., Leyton, F., Grandin, R., et al. (2014). Intense foreshocks and a slow slip event preceded the 2014 Iquique Mw 8.1 earthquake. *Science*, *345*, 1165–1169. https://doi.org/10.1126/science.1256074

Scholz, C. H. (1998). Earthquakes and friction laws. *Nature*, *391*, 37–42. https://doi.org/10.1038/34097

Scholz, C. H. (2002). *The mechanics of earthquakes and faulting* (2nd ed.). Cambridge University Press.

Scholz, C. H., Sykes, L. R., & Aggarwal, Y. P. (1973). Earthquake prediction: A physical basis. *Science*, *181*, 803–810. https://doi.org/10.1126/science.181.4102.803

Segall, P., & Bradley, A. M. (2012). The role of thermal pressurization and dilatancy in controlling the rate of fault slip. *Journal of Applied Mechanics*, *79*. https://doi.org/10.1115/1.4005896

Segall, P., Rubin, A. M., Bradley, A. M., & Rice, J. R. (2010). Dilatant strengthening as a mechanism for slow slip events. *Journal of Geophysical Research*, *115*. https://doi.org/10.1029/2010JB007449

Shelly, D. R. (2010). Periodic, chaotic, and doubled earthquake recurrence intervals on the deep San Andreas Fault. *Science*, *328*, 1385–1388. https://doi.org/10.1126/science.1189741

Sinha, N., Singh, A. K., Tiwari, D. K., & Vasudeo, A. D. (2019). *The effect of dilatancy, thermal-pressurization and hydraulic diffusivity on stick-slip instability and rock slope failure* (pp. 574–577). Presented at the INCAM.

Socquet, A., Valdes, J. P., Jara, J., Cotton, F., Walpersdorf, A., Cotte, N., et al. (2017). An 8 month slow slip event triggers progressive nucleation of the 2014 Chile megathrust. *Geophysical Research Letters*, *44*, 4046–4053. https://doi.org/10.1002/2017GL073023

Suzuki, T., & Yamashita, T. (2014). Effects of shear heating, slip-induced dilatancy and fluid flow on diversity of 1-D dynamic earthquake slip. *Journal of Geophysical Research: Solid Earth*, *119*, 2100–2120. https://doi.org/10.1002/2013JB010871

Tal, Y., Goebel, T., & Avouac, J.-P. (2020). Experimental and modeling study of the effect of fault roughness on dynamic frictional sliding. *Earth and Planetary Science Letters*, *536*, 116133. https://doi.org/10.1016/j.epsl.2020.116133

Tal, Y., Hager, B. H., & Ampuero, J. P. (2018). The effects of fault roughness on the earthquake nucleation process. *Journal of Geophysical Research: Solid Earth*, *123*, 437–456. https://doi.org/10.1002/2017JB014746

Tehseen, R., Farooq, M. S., & Abid, A. (2020). Earthquake prediction using expert systems: A systematic mapping study. *Sustainability*, *12*, 1–32. https://doi.org/10.3390/su12062420

Tokuda, T., & Shimada, H. (2019). Classes of low-frequency earthquakes based on inter-time distribution reveal a precursor event for the 2011 Great Tohoku Earthquake. *Scientific Reports*, *9*, 1–14. https://doi.org/10.1038/s41598-019-45765-0

Urata, Y., Kuge, K., & Kase, Y. (2012). Spontaneous dynamic rupture propagation beyond fault discontinuities: Effect of thermal pressurization. *Bulletin of the Seismological Society of America*, *102*, 53–63. https://doi.org/10.1785/0120110089

Wallace, L. M. (2020). Slow slip events in New Zealand. *Annual Review of Earth and Planetary Sciences*, *48*, 175–203. https://doi.org/10.1146/annurev-earth-071719-055104

Wei, M., Kaneko, Y., Liu, Y., & McGuire, J. J. (2013). Episodic fault creep events in California controlled by shallow frictional heterogeneity. *Nature Geoscience*, *6*, 566–570. https://doi.org/10.1038/ngeo1835

Wibberley, C. A. J. (2008). *The internal structure of fault zones: Implications for mechanical and fluid-flow properties*. Geological Society of London.

Yoshioka, N., & Scholz, C. H. (1989). Elastic properties of contacting surfaces under normal and shear loads: 1. Theory. *Journal of Geophysical Research*, *94*, 17681–17690. https://doi.org/10.1029/JB094iB12p17681

Zielke, O., Galis, M., & Mai, P. M. (2017). Fault roughness and strength heterogeneity control earthquake size and stress drop. *Geophysical Research Letters*, *44*, 777–783. https://doi.org/10.1002/2016GL071700

Zigone, D., Rivet, D., Radiguet, M., Campillo, M., Voisin, C., Cotte, N., et al. (2012). Triggering of tremors and slow slip event in Guerrero, Mexico, by the 2010 Mw 8.8 Maule, Chile, earthquake. *Journal of Geophysical Research*, *117*. https://doi.org/10.1029/2012JB009160

Reference From the Supporting Information

Caniven, Y., Morgan, J.K. & Blank, D.G. (2021). Datasets and movies supporting works on The Role of Along-Fault Dilatancy in Fault Slip Behavior [Data set]. *Zenodo*. https://doi.org/10.5281/zenodo.471466